Depth-resolved charge reconstruction at the LaNiO₃/CaMnO₃ interface

R. U. Chandrasena,[1,2] C. L. Flint,[3,4] W. Yang,[1,2] Arian Arab,[1,2] S. Nemšák,[5,6] M. Gehlmann,[6] V. B. Özdöl,[7] F. Bisti,[8]
K. D. Wijesekara,[1,2] J. Meyer-Ilse,[5] E. Gullikson,[5] E. Arenholz,[5] J. Ciston,[7] C. M. Schneider,[6] V. N. Strocov,[8]
Y. Suzuki,[4,9] and A. X. Gray[1,2,*]

[1]*Department of Physics, Temple University, 1925 North 12th Street, Philadelphia, Pennsylvania 19122, USA*
[2]*Temple Materials Institute, Temple University, 1925 North 12th Street, Philadelphia, Pennsylvania 19122, USA*
[3]*Department of Materials Science and Engineering, Stanford University, Stanford, California 94305, USA*
[4]*Geballe Laboratory for Advanced Materials, Stanford University, Stanford, California 94305, USA*
[5]*Advanced Light Source, Lawrence Berkeley National Laboratory, Berkeley, California 94720, USA*
[6]*Peter Grünberg Institut (PGI-6), Forschungszentrum Jülich GmbH, D-52425 Jülich, Germany*
[7]*National Center for Electron Microscopy, Molecular Foundry, Lawrence Berkeley National Laboratory, Berkeley, California 94720, USA*
[8]*Swiss Light Source, Paul Scherrer Institute, CH-5232 Villigen, Switzerland*
[9]*Department of Applied Physics, Stanford University, Stanford, California 94305, USA*

Rational design of low-dimensional electronic phenomena at oxide interfaces is currently considered to be one of the most promising schemes for realizing new energy-efficient logic and memory devices. An atomically abrupt interface between paramagnetic LaNiO₃ and antiferromagnetic CaMnO₃ exhibits interfacial ferromagnetism, which can be tuned via a thickness-dependent metal-insulator transition in LaNiO₃. Once fully understood, such emergent functionality could turn this archetypal Mott-interface system into a key building block for the above-mentioned future devices. Here, we use depth-resolved standing-wave photoemission spectroscopy in conjunction with scanning transmission electron microscopy and x-ray absorption spectroscopy, to demonstrate a depth-dependent charge reconstruction at the LaNiO₃/CaMnO₃ interface. Our measurements reveal an increased concentration of Mn^{3+} and Ni^{2+} cations at the interface, which create an electronic environment favorable for the emergence of interfacial ferromagnetism mediated via the Mn^{4+}-Mn^{3+} ferromagnetic double exchange and Ni^{2+}-O-Mn^{4+} superexchange mechanisms. Our findings suggest a strategy for designing functional Mott oxide heterostructures by tuning the interfacial cation characteristics via controlled manipulation of thickness, strain, and ionic defect states.

I. INTRODUCTION

Multifunctional complex-oxide heterostructures have been identified as candidate materials systems that may enable the coupling of electronic logic with magnetic memory and lead to the next generation of spintronic devices [1–5]. Among the many complex-oxide heterostructures studied to date, there has been a class of heterostructures where the interfaces give rise to functional properties not observed in the constituent materials [6]. With many such emergent properties, ranging from interfacial metallicity [7–9] to interfacial superconductivity [10,11], there has been only a handful of successful efforts demonstrating new magnetic ground states at interfaces [12,13]. One such example is the LaNiO₃/CaMnO₃ system where the ferromagnetic ground state emerges at the interface, although LaNiO₃ is a paramagnetic metal and CaMnO₃ is an antiferromagnetic insulator in the bulk [13–15].

The emergence of interfacial ferromagnetism in the LaNiO₃/CaMnO₃ system has been attributed to two distinct mechanisms: a Mn^{4+}-Mn^{3+} double exchange interaction in the interfacial CaMnO₃ layer and a Ni^{2+}-O-Mn^{4+} superexchange interaction at the interface between the LaNiO₃ and

CaMnO₃ [13–15]. The relative importance of the two mechanisms depends on the thickness of the individual layers due to a thickness-dependent metal-insulator transition in the LaNiO₃ layer [16–18]. The transition, which occurs in the ultrathin (few-unit-cell) limit, determines which is the dominant mechanism for the mediation of the ferromagnetic coupling. Such tunability provides an ideal platform for studying fundamental interactions leading to emergent magnetism at oxide interfaces and makes this heterostructure a potential candidate for the above-mentioned devices [12,19,20].

Both of the above-mentioned mechanisms require an interfacial charge reconstruction, which results in the presence of the transition-metal cations with the valence states other than the formal valence state of the stoichiometric compounds ($LaNi^{3+}O_3$ and $CaMn^{4+}O_3$). Such charge reconstruction, resulting in the formation of off-stoichiometric cations (Ni^{2+} and Mn^{3+}) at the interface, can be explained in terms of the charge leakage from LaNiO₃ to CaMnO₃ [13–15], as well as the presence of oxygen vacancies driven to the interface by polar compensation [21–24]. Both scenarios are plausible in the LaNiO₃/CaMnO₃ heterostructures. Specifically, in metallic superlattices with near- and above-critical LaNiO₃ thicknesses, leakage of itinerant Ni 3d e_g electrons into the interfacial CaMnO₃ layer is expected to reduce the valence state of some of the interfacial Mn cations from 4+ to 3+, leading
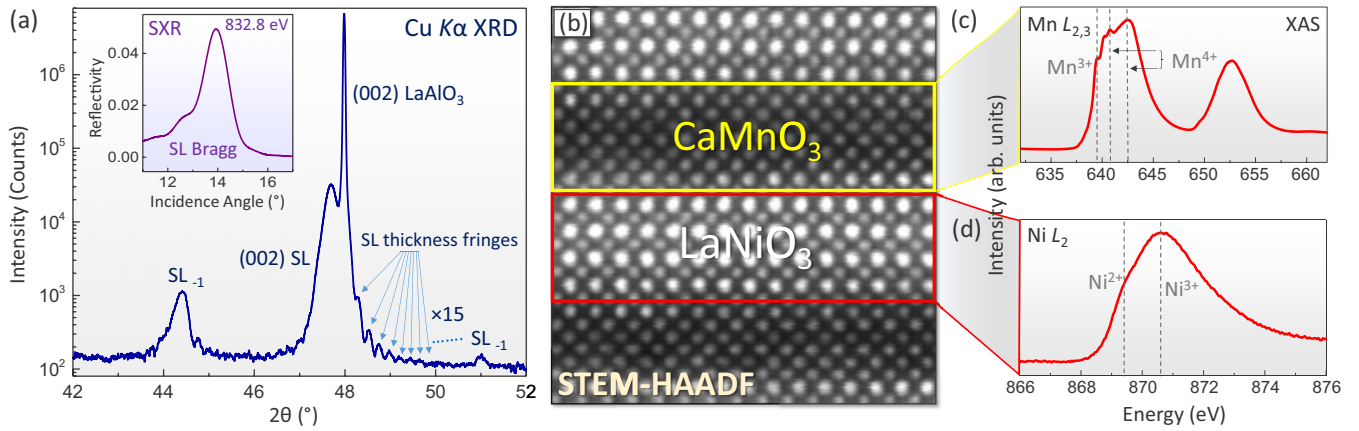
*axgray@temple.edu

FIG. 1. (a) XRD 2θ-θ spectrum around the LaAlO$_3$ (002) peak showing clearly resolved SL thickness fringes, as well as the first-order SL Bragg peaks. Inset: Synchrotron-based SXR spectrum (at $h\nu = 832.8$ eV) of the first-order superlattice Bragg peak in the soft-x-ray regime. (b) High-resolution STEM-HAADF cross-sectional image of the superlattice sample showing a typical atomically abrupt LaNiO$_3$/CaMnO$_3$ interface. (c, d) XAS spectra probing the CaMnO$_3$ layer at the Mn $L_{2,3}$ absorption edges (c) and the LaNiO$_3$ layer at the Ni L_2 edge (d) revealing mixed valence states for the Mn (3+ and 4+) and Ni (2+ and 3+) cations in the respective layers.

to the emergence of interfacial ferromagnetism mediated by the Mn^{4+}-Mn^{3+} double exchange interaction [13–15,25]. This scenario has been theoretically predicted and discussed in-depth in prior experimental studies [13–15] and could explain the observed link between the thickness-dependent metal-insulator transition in ultrathin LaNiO$_3$ and the observed suppression of ferromagnetism in the superlattices with near- and below-critical-thickness LaNiO$_3$ layers (see Fig. 2 in Ref. [15]). In superlattices with thinner LaNiO$_3$, which is closer to the metal-insulator transition and hence has more resistive transport properties, Ni^{2+}-O-Mn^{4+} superexchange interaction (made possible by oxygen vacancies driven to the interface) has been identified as the source of the interfacial ferromagnetism [14,15]. On the other hand, oxygen vacancies have also been observed in coherently strained epitaxial CaMnO$_3$ [21] and LaNiO$_3$ [22–24] and, in some cases, have been both predicted and observed to segregate at the interfaces due to polar energetics at the interface [22,23].

Gaining a clear picture of the depth-dependent evolution of materials' electronic properties, valence states, and charge redistribution across the interface is therefore required to determine the roles of double exchange and superexchange interactions in the emergence of the observed interfacial ferromagnetism in this system. Thus, here, we used a combination of depth-resolved soft-x-ray standing-wave photoemission spectroscopy (SW-XPS), x-ray absorption spectroscopy (XAS), and scanning transmission electron microscopy (STEM) to selectively probe the interface electronic structure and valence states of the relevant transition-metal cations (Mn and Ni). Our results reveal an increased concentration of Mn^{3+} and Ni^{2+} cations at the LaNiO$_3$/CaMnO$_3$ interface, indicating the coexistence of competing Mn^{3+}-Mn^{4+} double exchange with Ni^{2+}-O-Mn^{4+} superexchange interactions that give rise to emergent interfacial ferromagnetism.

II. EXPERIMENT

For this paper, a high-quality epitaxial [4-u.c. LaNiO$_3$/ 4-u.c. CaMnO$_3$] × 15 superlattice was synthesized on top of

a single-crystalline LaAlO$_3$ (001) substrate using pulsed laser deposition. Layer-by-layer growth was monitored *in situ* using reflection high-energy electron diffraction. After deposition, coherent epitaxy, crystallinity, and layering of the superlattice were verified using *ex situ* x-ray-diffraction spectroscopy (XRD), soft-x-ray reflectivity (SXR), as well as STEM (see Fig. 1). Bulk magnetization and electronic transport measurements, carried out by us in a prior study on similar samples [15], revealed a ferromagnetic signal (0.3 μB/Int.Mn at 10 K) and temperature-dependent resistivity (4×10^{-4} Ω cm at 10 K), which is consistent with the onset of metallicity in LaNiO$_3$. More details regarding the deposition process and sample characterization can be found in Ref. [15].

A high-angular-resolution ($<0.01°$) XRD 2θ-θ spectrum in Fig. 1(a), recorded using a Bruker D8 Discover diffractometer, shows well-resolved superlattice (SL) period thickness fringes and Bragg peaks, thus attesting to the high quality and precise control of the SL synthesis. A high-angular-resolution ($<0.01°$) SXR spectrum (see inset), recorded at the Calibration and Standards beamline 6.3.2 of the Advanced Light Source (LBNL), confirms the presence and the angular position of the SL Bragg peak in the soft-x-ray regime at the photon energy used for the SW-XPS measurements described below.

At the atomic level, the high-angle annular dark-field (HAADF) STEM image in Fig. 1(b), recorded using the aberration-corrected TEAM I microscope at the National Center for Electron Microscopy Facility of the Molecular Foundry (LBNL), shows several typical atomically abrupt interfaces between LaNiO$_3$ and CaMnO$_3$. The A-site (La and Ca) atomic columns can be easily differentiated due to the high atomic number contrast, with the heavier cations (La) appearing brighter. The interfacial layers show some fluctuations in atomic column intensity of the A sites, suggesting that the interfacial mixing is confined to a single unit cell, consistent with a prior study on similar samples [13].

The high-resolution (100 meV) XAS spectra of the Mn $L_{2,3}$ and Ni L_2 absorption edges, recorded in the total electron yield (TEY) detection mode at the Magnetic Spectroscopy
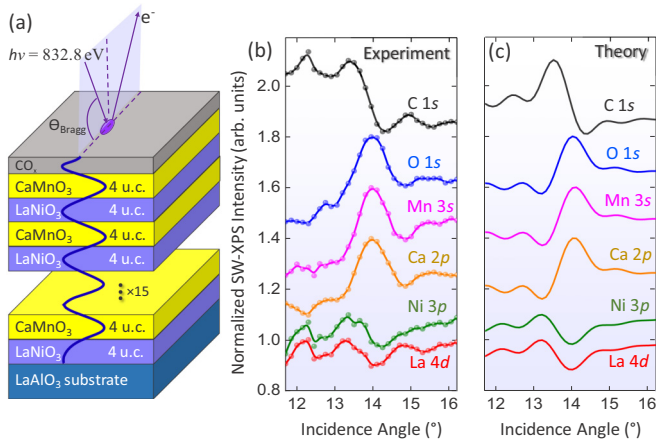
FIG. 2. (a) Schematic diagram of the investigated superlattice structure consisting of 15 $LaNiO_3$/$CaMnO_3$ bilayers, grown epitaxially on a single-crystal $LaAlO_3$ substrate, with each bilayer consisting of four unit cells of $LaNiO_3$ and four unit cells of $CaMnO_3$. An excitation photon energy of 832.8 eV, corresponding to the onset of the La $3d_{5/2}$ absorption threshold, was utilized for the photoemission experiments to enhance the standing-wave modulation amplitude at the Bragg condition. (b) Experimental core-level photoemission intensity rocking curves for all elements in the superlattice and (c) best theoretical fits to the data.

beamline of the Advanced Light Source (LBNL) [26], reveal fine spectral features attributed to the Mn^{3+} and Mn^{4+} cations at 640 and 643 eV, respectively [Fig. 1(c)] [21], as well as the Ni^{2+} (869.5 eV) and Ni^{3+} (870.5 eV) peak components at the Ni L_2 edge [Fig. 1(d)] [27–29]. The data thus suggest a mixture of Mn^{3+} and Mn^{4+} cations originating in the $CaMnO_3$ layer and a mixture of Ni^{2+} and Ni^{3+} cations originating in the $LaNiO_3$ layer. However, XAS-TEY is a depth-averaging spectroscopic technique with a typical probing depth of 5 nm [30,31], and thus does not provide a depth-resolved valence-state profile of the structure with sufficient resolution.

Thus, in order to selectively probe the electronic structure and valence states of the Mn and Ni cations at the $LaNiO_3$/$CaMnO_3$ interface, we have carried out soft-x-ray SW-XPS measurements at the high-resolution ADRESS beamline of the Swiss Light Source [32,33]. The SX-ARPES end station at the ADRESS beamline was equipped with a SPECS PHOIBOS-150 hemispherical electrostatic analyzer and a six-axis cryogenic manipulator, allowing for optimal alignment of the sample and high-precision angle-resolved standing-wave measurements. The above-mentioned measurements were accomplished by setting up an x-ray standing-wave field within the periodic [4-u.c. $LaNiO_3$/4-u.c. $CaMnO_3$] × 15 superlattice sample, which in first-order Bragg reflection acted as the standing-wave generator [see Fig. 2(a)]. The antinodes of the standing wave were moved vertically through the sample by scanning (rocking) the x-ray incidence angle [34,35]. The sample temperature was set at 30 K.

The photon energy of 832.8 eV, just below the La $3d_{5/2}$ absorption threshold, was used to maximize the x-ray reflectivity of the superlattice, which in turn enhanced the standing-wave modulation amplitude. In preparation for the experiment,

energy-dependent SXR measurements were carried out to fine tune the experimental parameters, such as the optimal photon energy and the angular range for the x-ray incidence [see inset in Fig. 1(a)].

III. RESULTS AND DISCUSSION

Core-level photoemission intensities from every constituent element of the superlattice (La $4d$, Ni $3p$, Ca $2p$, Mn $3s$, O $1s$, and C $1s$) were recorded as a function of grazing incidence angle from 11.7 to 16.2° [see Fig. 2(b)] and self-consistently fitted using an x-ray optical theoretical code [36], which accounts for the differential photoelectric cross section as well as the inelastic mean free paths of photoelectrons inside the sample. Only the thicknesses of the $CaMnO_3$ and $LaNiO_3$ layers and the interdiffusion between them were allowed to vary in the model. The x-ray optical constants needed for the calculations were obtained via XAS and Kramer-Kronig analysis [34]. Figure 2(c) shows the best theoretical fits to the experimental data, exhibiting excellent agreement in terms of the amplitudes, relative phases, and shapes. Surface-adsorbed CO_x contaminant from the exposure to atmosphere provides an excellent depth reference (black spectrum), thus further constraining the fitting and the calculations.

A detailed structure of the topmost layers derived from the experiment, as well as the simulated intensity of the x-ray standing-wave electric field (E^2) as a function of depth inside the sample and of x-ray incidence angle, are shown in Fig. 3(a) and were obtained by using the set of best-fit parameters. Resultant thicknesses of the 4-u.c.-thick layers of $LaNiO_3$ (15.55 Å) and $CaMnO_3$ (14.80 Å) are consistent with the unit-cell thicknesses of 3.89 Å ($LaNiO_3$) and 3.73 Å ($CaMnO_3$), reported previously in the literature [37–39].

The E^2 profile simulation shown in Fig. 3(a) indicates that at lower incidence angles (yellow vertical line at ∼13.3°) the two antinodes of the standing wave highlight predominantly the top and the bottom interfaces of the $CaMnO_3$ film (regions marked with letters "a"), while the middle "bulklike" section of the film resides in the dark region (SW node). With increasing incidence angle, the top antinode propagates downward into the $CaMnO_3$ layer spreading over almost the entire four unit cells at around 14.4° (marked with another yellow vertical line) with the maximum intensity at approximately the center of the layer (region marked with letter "b"). Such contrasting angle-dependent depth distribution of the probing x-ray E-field intensities within the sample enables clear differentiation between the bulklike and "interfacelike" species of Mn in the $CaMnO_3$ layer, as well as a particular sensitivity to the interfacelike Ni in the $LaNiO_3$ buried layer. Importantly, the simulation results indicate that the standing-wave contrast within the topmost layers of the sample is strong, reaching a maximum difference of approximately 53% between the values of E^2 in the nodes and antinodes of the SW [see the color scale in Fig. 3(a)]. Additional line cuts, showing E-field intensity profiles at several key incidence angles, are shown in Fig. S1 in the Supplemental Material [40].

In order to determine the valence-state profiles of the key cations, we examine the line shapes of the Mn $3s$ and Ni $3p$ core-level spectra at the x-ray grazing incidence
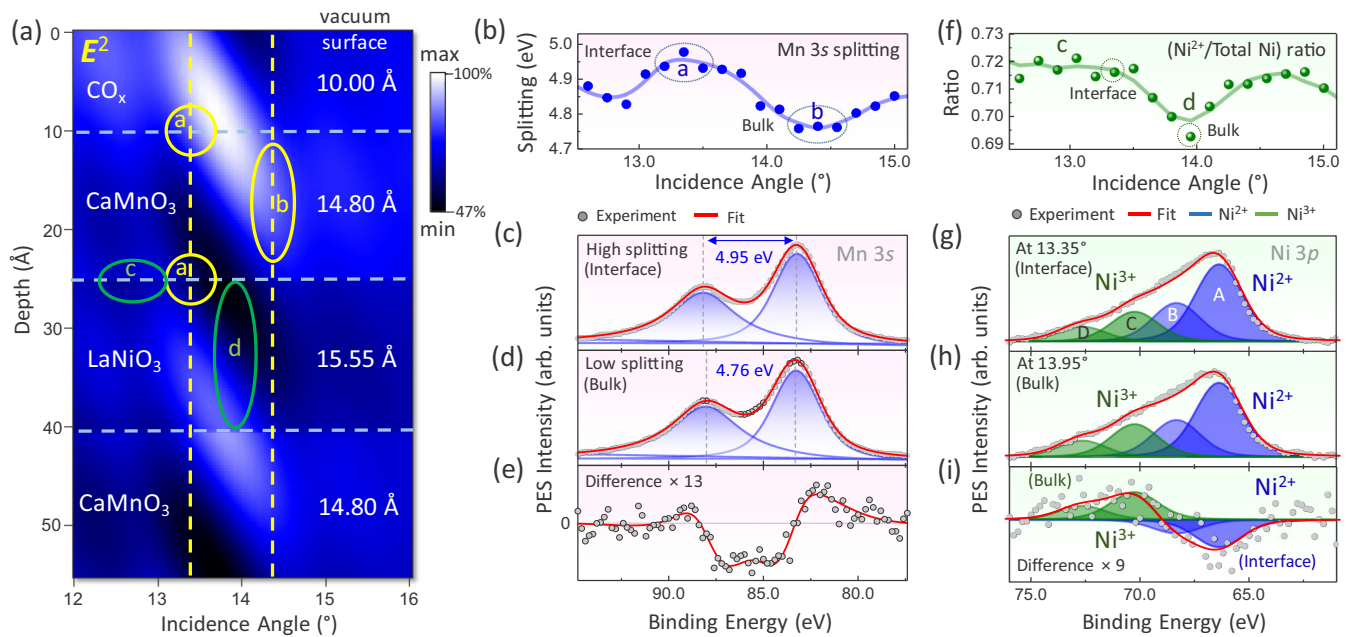
FIG. 3. (a) Simulated intensity of the x-ray standing-wave electric field (E^2) inside the superlattice as a function of depth (vertical axis) and x-ray grazing incidence angle (horizontal axis). Calculated layer thicknesses shown on the right are consistent with the $4 \times$ multiples of the $LaNiO_3$ and $CaMnO_3$ unit-cell constants reported in the literature [37–39]. (b) Depth dependent evolution of the Mn $3s$ multiplet splitting (in eV) as a function of the x-ray grazing incidence angle. (c, d) Mn $3s$ core-level photoemission spectra recorded in the interface-sensitive ($\sim$13.3°) and bulk-sensitive ($\sim$14.4°) experimental geometries, respectively. (e) Difference spectrum obtained by subtracting the spectrum obtained at $\sim$13.3° (c) from that obtained at $\sim$14.4° (d). (f) Plot of the relative Ni^{2+} peak(s) intensity as a function of x-ray grazing incidence angle. (g, h) Ni $3p$ core-level photoemission spectra recorded at $\sim$13.35 and $\sim$13.95° respectively. (i) "Bulk−interface" difference spectrum obtained by subtracting the spectrum obtained at $\sim$13.35° (g) from that obtained at $\sim$13.95° (h).

angles corresponding to the interface-sensitive and bulk-sensitive standing-wave configurations. Conventional photoemission spectra for typical bulklike stoichiometric or near-stoichiometric $CaMnO_3$ and $LaNiO_3$ thin films are provided for reference in Fig. S2 in the Supplemental Material [40].

Figure 3(b) depicts the depth-dependent evolution of the Mn $3s$ core-level multiplet splitting (in eV) as function of x-ray incidence angle. The magnitude of the $3s$ splitting decreases monotonically with the increase of the formal valency of the Mn cation [41,42], and is thus often used as a reliable and highly sensitive experimental observable for determining the Mn valence state [21,42]. In the $CaMnO_3$-interface sensitive experimental geometry, at the x-ray incidence angles between 13.2 and 13.5° (corresponding to region a in the sample), the average splitting is estimated to be 4.95 eV, after self-consistent Shirley-background subtraction and peak fitting [see Fig. 3(c)]. This value of splitting corresponds to the formal Mn valency of approximately +3.4 [41], thus suggesting a mixture of Mn^{+3} and Mn^{+4} cations, with predominantly Mn^{3+} ion content at the interface.

For higher x-ray incidence angles, as the SW antinode propagates toward the center of the $CaMnO_3$ layer [as shown in Fig. 3(a)], the Mn $3s$ splitting gradually decreases, reaching a value of 4.76 eV [see Fig. 2(c)] in the $CaMnO_3$-bulk sensitive geometry, at the incidence angle of $\sim$14.4° (corresponding to region b in the sample). For this magnitude of the $3s$ splitting, formal valency of the Mn cations is estimated to be approximately +3.6 [41], which suggests an increase of

the Mn^{+4} ion concentration (as in stoichiometric $CaMnO_3$) toward the bulk of the layer.

The difference spectrum in Fig. 3(e), comparing Mn $3s$ spectra in the interface-sensitive and bulk-sensitive experimental geometries, exhibits a line shape that is typical of the increasing splitting, with positive incursions at 82 and 88 eV and a negative dip emerging between the two separated multiplet components. The observed change in the Mn $3s$ splitting (190 meV) is approximately a factor of 2 larger as compared to the total experimental energy resolution ($\sim$100 meV).

A conventional surface-sensitive XPS spectrum recorded with the same photon energy but away from the Bragg condition shows that the value of the Mn $3s$ splitting measured near the surface is 4.81 eV, which is close to the bulklike value of 4.76 eV (see Fig. S3 in the Supplemental Material [40]). The splitting increases significantly to 4.95 eV (becomes more Mn^{3+}-like) only when the additional standing-wave intensity highlights the bottom (buried) interface with $LaNiO_3$.

In summary, our experimental SW-XPS results, in conjunction with x-ray optical modeling, indicate an increased concentration of Mn^{3+} cations in the interfacial regions of the $CaMnO_3$ film. Evidence of such charge reconstruction has been observed indirectly in prior studies using depth-averaging techniques [13,15]. There are two possible sources of Mn^{3+} at the interfaces: the leakage of itinerant electrons from the $LaNiO_3$ to the $CaMnO_3$ and the segregation of oxygen vacancies in $CaMnO_3$ to the interfaces. The temperature-dependent resistivity data suggest the onset of metallicity in

superlattices with 4-u.c.-thick $LaNiO_3$ layers, with increasingly lower resistivities in superlattices with thicker $LaNiO_3$ layers (e.g., 6–8 u.c.—see Fig. 2 in Ref. [15]). Therefore the mechanism of the leakage of itinerant electrons from $LaNiO_3$ into the first $CaMnO_3$ layer is the likely explanation in our superlattice. With increasing metallicity of the $LaNiO_3$ layers, the emergent interfacial ferromagnetism is dominated by the Mn^{4+}-Mn^{3+} double exchange interaction mediated by the leakage of the itinerant electrons and not Ni^{2+}-O-Mn^{4+} superexchange interactions.

Mn^{3+}-Mn^{4+} disproportionation at the interface is predicted to stabilize Mn^{4+}-Mn^{3+} double-exchange ferromagnetism, various signatures of which have been observed via bulk magnetometry, polarization-dependent XAS, and polarized neutron reflectometry [13,15]. The latter technique provides a depth-resolved profile of magnetization in the superlattice and has shown that ferromagnetism in the $CaMnO_3$ film is confined to one unit cell at the interface with $LaNiO_3$, in agreement with our conclusions [13]. Our depth-resolved SW-XPS results thus provide a direct experimental link between the emergent magnetic and electronic interfacial properties and represent strong evidence to support the model of Mn^{4+}-Mn^{3+} double-exchange-mediated ferromagnetism in the $LaNiO_3$/$CaMnO_3$ superlattices.

The emergence of interfacial ferromagnetism mediated by the Ni^{2+}-O-Mn^{4+} superexchange interactions requires the presence of off-stoichiometric Ni^{2+} cations at the interface. In Figs. 3(f)–3(i), we show the depth-dependent evolution of several features of the Ni $3p$ core-level peak, which have been used in numerous prior studies to determine the Ni valence state in $LaNiO_3$ [43,44] and related compounds [45]. We label these components A–D in Fig. 3(g), in accordance with the convention used by Qiao and Bi [see Fig. S2(b) from Ref. [43]]. Features A and C can be assigned to the Ni^{2+} $3p_{3/2}$ and Ni^{3+} $3p_{3/2}$, respectively, while B and D are their $3p_{1/2}$ counterparts [43].

It is immediately apparent from Figs. 3(g) and 3(h) that the Ni^{2+} components (A and B) are more intense, as compared to the Ni^{3+} peaks (C and D). However, it is important to note that, due to the inelastic attenuation of the photoelectrons in the buried $LaNiO_3$ layer, at the photon energy of 832.8 eV we are mostly sensitive to the topmost interfacelike region of the film. In fact, with the inelastic mean free path estimated at $\sim$15 Å [46], intensity of the photoemission signal from the central bulklike region of the film is diminished by approximately 40%, compared to the photoemission signal originating from the top $LaNiO_3$/$CaMnO_3$ interface [46,47]. Thus, from the first evaluation of the $3p$ spectral line shapes in Figs. 3(g) and 3(h), we can conclude that the interface region of the buried $LaNiO_3$ film contains a significant concentration of the Ni^{2+} cations. For measurements carried out at incidence angles that are sufficiently far away from the Bragg condition to ensure almost uniform illumination of the film [12.5–13.3°, or region "c" in Fig. 3(a)], the relative intensity ratio (RIR) of the Ni^{2+} peak components to the total $3p$ intensity is estimated to be $\sim$0.71 [see Fig. 3(f)].

Remarkably, in the Bragg condition, a SW node (dark spot) appears at the $LaNiO_3$/$CaMnO_3$ interface at $\sim$13.35° and propagates into the $LaNiO_3$ layer, thus suppressing the signal from the interface with a maximum effect at approximately
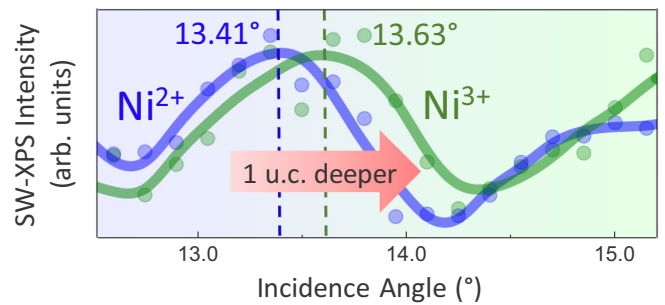

FIG. 4. Individual standing-wave rocking-curve modulations for the Ni^{2+} (blue) and Ni^{3+} (green) components of the Ni $3p$ core-level spectrum shown in Fig. 3(g). A relative shift of approximately +0.3° of the Ni^{3+} component with respect to the Ni^{2+} component corresponds to a 3.2-Å ($\sim$1-u.c.) increase in the depth position of the SW probe inside of the $LaNiO_3$ layer. Circles correspond to experimental data and solid lines are guides to the eye obtained via polynomial fitting of the data.

14.0° [region "d" in Fig. 3(a)]. Within the same angular range of $\sim$13.3−14.0°, an antinode (bright spot) appears in the central region of the film, thus enhancing the signal from the bulklike $LaNiO_3$. Our data in Fig. 3(e) reveal that such enhancement of the bulklike signal (and simultaneous suppression of the interfacelike signal) results in a significant drop of the Ni^{2+} RIR and an increase in the relative Ni^{3+} peak intensities. A difference plot, comparing Ni $3p$ spectra in the interface-sensitive and bulk-sensitive experimental geometries, highlights this depth-dependent disproportionation of the Ni valence states [Fig. 3(i)].

An effective way of confirming the above-described depth-dependent disproportionation of the Ni species within the $LaNiO_3$ layer is to compare the line shapes of the rocking curves (RCs) for the Ni^{2+} (A+B, blue) and Ni^{3+} (C+D, green) individual components. Figure 4 reveals a clear shift to a higher grazing incidence angle of the entire Ni^{3+} component RC, relative to the Ni^{2+} RC. Such angular shift (estimated at approximately 0.3°) corresponds to a $\sim$3.2-Å (about one unit cell) increase in the depth position of the SW probe inside of the $LaNiO_3$ layer. Thus, the difference in the angular characteristics of the rocking curves in Fig. 4 suggests that the Ni^{2+} components of the Ni $3p$ spectrum originate mainly from the interfacial region with $CaMnO_3$, while the Ni^{3+} signal comes mainly from the deeper bulklike $LaNiO_3$ layers.

Evidence of such interfacial charge redistribution has been observed in a prior combined XAS and resonant soft-x-ray scattering study on similar superlattices [15] and is consistent with the polar compensation picture [15,22], wherein polar mismatch at the $LaNiO_3$/$CaMnO_3$ interface leads to interfacial Ni^{2+} cations in the polar $LaNiO_3$ layer through the formation of oxygen vacancies. The ensuing interaction between the interfacial Ni^{2+} and adjacent Mn^{4+} on the $CaMnO_3$ side of the interface is predicted to stabilize the ferromagnetic ground state via the superexchange mechanism [48,49]. Our depth-resolved SW-XPS results support this model and suggest that this interaction is likely confined to a narrow (one unit cell) region at the interface.

IV. CONCLUSIONS

In conclusion, in this paper we used SW-XPS in conjunction with x-ray optical modeling to determine the valence-state profile of the Mn and Ni cations at an atomically abrupt epitaxial 4-u.c. $LaNiO_3$/4-u.c. $CaMnO_3$ interface—a potential building block for next-generation spintronic devices. By looking at the depth-resolved evolution of the spectral line shapes of the Mn $3s$ and Ni $3p$ core levels, we observed an increased concentration of Mn^{3+} and Ni^{2+} cations at the buried interface. Concomitantly, the "formal valence" cations (Mn^{4+} and Ni^{3+}) were shown to be more abundant in the bulklike regions of the respective films. The observed depth-dependent charge redistribution creates an electronic environment favorable for the emergence of interfacial ferromagnetism mediated via the Mn^{4+}-Mn^{3+} ferromagnetic double exchange and Ni^{2+}-O-Mn^{4+} superexchange mechanisms. The competition between these two mechanisms can be influenced by tuning the thickness of the $LaNiO_3$ layer, which undergoes a metal-insulator transition in the ultrathin limit (<4 u.c.), resulting in the thickness-dependent controllability of the magnetic moment at the interface as demonstrated in a prior study [15].

[1] R. Ramesh and N. A. Spaldin, Nat. Mater. **6**, 21 (2007).

[2] J. M. Rondinelli, M. Stengel, and N. A. Spaldin, Nat. Nanotechnol. **3**, 46 (2007).

[3] M. Bibes, J. E. Villegas, and A. Barthélémy, Adv. Phys. **60**, 5 (2011).

[4] P. Zubko, S. Gariglio, M. Gabay, P. Ghosez, and J.-M. Triscone, Annu. Rev. Condens. Matter Phys. **2**, 141 (2011).

[5] S. Fusil, V. Garcia, A. Barthélémy, and M. Bibes, Annu. Rev. Mater. Res. **44**, 91 (2014).

[6] H. Y. Hwang, Y. Iwasa, M. Kawasaki, B. Keimer, N. Nagaosa, and Y. Tokura, Nat. Mater. **11**, 103 (2012).

[7] P. Moetakef, J. Y. Zhang, A. Kozhanov, B. Jalan, R. Seshadri, S. J. Allen, and S. Stemmer, Appl. Phys. Lett. **99**, 232116 (2011).

[8] A. Ohtomo and H. Y. Hwang, Nature (London) **427**, 423 (2004).

[9] A. Ohtomo, D. A. Muller, J. L. Grazul, and H. Y. Hwang, Nature (London) **419**, 378 (2002).

[10] A. Gozar, G. Logvenov, L. F. Kourkoutis, A. T. Bollinger, L. A. Giannuzzi, D. A. Muller, and I. Bozovic, Nature (London) **455**, 782 (2008).

[11] N. Reyren, S. Thiel, A. D. Caviglia, L. Fitting Kourkoutis, G. Hammerl, C. Richter, C. W. Schneider, T. Kopp, A.-S. Rüetschi, D. Jaccard, M. Gabay, D. A. Muller, J.-M. Triscone, and J. Mannhart, Science **317**, 1196 (2007).

[12] K. S. Takahashi, M. Kawasaki, and Y. Tokura, Appl. Phys. Lett. **79**, 1324 (2001).

[13] A. J. Grutter, H. Yang, B. J. Kirby, M. R. Fitzsimmons, J. A. Aguiar, N. D. Browning, C. A. Jenkins, E. Arenholz, V. V. Mehta, U. S. Alaan, and Y. Suzuki, Phys. Rev. Lett. **111**, 087202 (2013).

[14] C. L. Flint, A. Vailionis, H. Zhou, H. Jang, J. S. Lee, and Y. Suzuki, Phys. Rev. B **96**, 144438 (2017).

[15] C. L. Flint, H. Jang, J. S. Lee, A. T. N'Diaye, P. Shafer, E. Arenholz, and Y. Suzuki, Phys. Rev. Mater. **1**, 024404 (2017).

[16] R. Scherwitzl, S. Gariglio, M. Gabay, P. Zubko, M. Gibert, and J. M. Triscone, Phys. Rev. Lett. **106**, 246403 (2011).

[17] D. P. Kumah, A. S. Disa, J. H. Ngai, H. Chen, A. Malashevich, J. W. Reiner, S. Ismail- Beigi, F. J. Walker, and C. H. Ahn, Adv. Mater. **26**, 1935 (2014).

[18] S. Middey, J. Chakhalian, P. Mahadevan, J. W. Freeland, A. J. Millis, and D. D. Sarma, Annu. Rev. Mater. Res. **46**, 305 (2016).

[19] J. Hoffman, I. C. Tung, B. B. Nelson-Cheeseman, M. Liu, J. W. Freeland, and A. Bhattacharya, Phys. Rev. B **88**, 144411 (2013).

[20] A. Bhattacharya and S. J. May, Annu. Rev. Mater. Res. **44**, 65 (2014).

[21] R. U. Chandrasena, W. Yang, Q. Lei, M. U. Delgado-Jaime, K. D. Wijesekara, M. Golalikhani, B. A. Davidson, E. Arenholz, K. Kobayashi, M. Kobata, F. M. F. de Groot, U. Aschauer, N. A. Spaldin, X. X. Xi, and A. X. Gray, Nano Lett. **17**, 794 (2017).

[22] I. C. Tung, I.-C. Tung, G. Luo, J. H. Lee, S. H. Chang, J. Moyer, H. Hong, M. J. Bedzyk, H. Zhou, D. Morgan, D. D. Fong, and J. W. Freeland, Phys. Rev. Mater. **1**, 053404 (2017).

[23] M. Anada, K. Kowa, H. Maeda, E. Sakai, M. Kitamura, H. Kumigashira, O. Sakata, Y. Nakanishi-Ohno, M. Okada, T. Kimura, and Y. Wakabayashi, Phys. Rev. B **98**, 014105 (2018).

[24] M. Golalikhani, Q. Lei, R. U. Chandrasena, L. Kasaei, H. Park, J. Bai, P. Orgiani, J. Ciston, G. E. Sterbinsky, D. A. Arena, P. Shafer, E. Arenholz, B. A. Davidson, A. J. Millis, A. X. Gray, and X. X. Xi, Nat. Commun. **9**, 2206 (2018).

[25] B. R. K. Nanda, S. Satpathy, and M. S. Springborg, Phys. Rev. Lett. **98**, 216804 (2007).

[26] A. T. Young, E. Arenholz, J. Feng, H. Padmore, S. Marks, R. Schlueter, E. Hoyer, N. Kelez, and C. Steier, Surf. Rev. Lett. **09**, 549 (2002).

[27] S. Middey, D. Meyers, M. Kareev, E. J. Moon, B. A. Gray, X. Liu, J. Freeland, and J. Chakhalian, Appl. Phys. Lett. **101**, 261602 (2012).

[28] Y. Bitla, Y. Y. Chin, J. C. Lin, C. N. Van, R. Liu, Y. Zhu, H.-J. Liu, Q. Zhan, H. J. Lin, C. T. Chen, Y. H. Chu, and Q. He, Sci. Rep. **5**, 15201 (2015).

[29] Y. Yokoyama, D. Ootsuki, T. Sugimoto, H. Wadati, J. Okabayashi, X. Yang, F. Du, G. Chen, and T. Mizokawa, Appl. Phys. Lett. **107**, 033903 (2015).

[30] N. B. Aetukuri, A. X. Gray, M. Drouard, M. Cossale, L. Gao, A. H. Reid, R. Kukreja, H. Ohldag, C. A. Jenkins, E. Arenholz, K. P. Roche, H. A. Dürr, M. G. Samant, and S. S. P. Parkin, Nat. Phys. **9**, 661 (2013).

[31] E. Arenholz, G. van der Laan, R. V. Chopdekar, and Y. Suzuki, Phys. Rev. B **74**, 094407 (2006).

[32] V. N. Strocov, X. Wang, M. Shi, M. Kobayashi, J. Krempasky, C. Hess, T. Schmitt, and L. Patthey, J. Synchrotron Rad. **21**, 32 (2014).

[33] V. N. Strocov, T. Schmitt, U. Flechsig, T. Schmidt, A. Imhof, Q. Chen, J. Raabe, R. Betemps, D. Zimoch, J. Krempasky, X. Wang, M. Grioni, A. Piazzalunga, and L. Patthey, J. Synchrotron Rad. **17**, 631 (2010).

[34] A. X. Gray, C. Papp, B. Balke, S.-H. Yang, M. Huijben, E. Rotenberg, A. Bostwick, S. Ueda, Y. Yamashita, K. Kobayashi, E. M. Gullikson, J. B. Kortright, F. M. F. de Groot, G. Rijnders, D. H. A. Blank, R. Ramesh, and C. S. Fadley, Phys. Rev. B **82**, 205116 (2010).

[35] A. M. Kaiser, A. X. Gray, G. Conti, J. Son, A. Greer, A. Perona, A. Rattanachata, A. Y. Saw, A. Bostwick, S. Yang, S.-H. Yang, E. M. Gullikson, J. B. Kortright, S. Stemmer, and C. S. Fadley, Phys. Rev. Lett. **107**, 116402 (2011).

[36] S.-H. Yang, A. X. Gray, A. M. Kaiser, B. S. Mun, B. C. Sell, J. B. Kortright, and C. S. Fadley, J. Appl. Phys. **113**, 073513 (2013).

[37] J. Chakhalian, J. M. Rondinelli, Jian Liu, B. A. Gray, M. Kareev, E. J. Moon, N. Prasai, J. L. Cohn, M. Varela, I. C. Tung, M. J. Bedzyk, S. G. Altendorf, F. Strigari, B. Dabrowski, L. H. Tjeng, P. J. Ryan, and J. W. Freeland, Phys. Rev. Lett. **107**, 116805 (2011).

[38] M. C. Weber, M. Guennou, N. Dix, D. Pesquera, F. Sánchez, G. Herranz, J. Fontcuberta, L. López- Conesa, S. Estradé, F. Peiró, Jorge Iñiguez, and J. Kreisel, Phys. Rev. B **94**, 014118 (2016).

[39] C. L. Flint, A. J. Grutter, C. A. Jenkins, E. Arenholz, and Y. Suzuki, J. Appl. Phys. **115**, 17D712 (2014).

[40] See Supplemental Material at http://link.aps.org/supplemental/10.1103/PhysRevB.98.155103 for additional simulations and reference spectra.

[41] V. R. Galakhov, M. Demeter, S. Bartkowski, M. Neumann, N. A. Ovechkina, E. Z. Kurmaev, N. I. Lobachevskaya, Ya. M. Mukovskii, J. Mitchell, and D. L. Ederer, Phys. Rev. B **65**, 113102 (2002).

[42] E. Beyreuther, S. Grafström, L. M. Eng, C. Thiele, and K. Dörr, Phys. Rev. B **73**, 155425 (2006).

[43] L. Qiao and X. Bi, Europhys. Lett. **93**, 57002 (2011).

[44] X. Ning, Z. Wang, and Z. Zhang, Sci. Rep. **5**, 8460 (2015).

[45] M. Burriel, S. Wilkins, J. P. Hill, M. A. Munoz-Marquez, H. H. Brongersma, J. A. Kilner, M. P. Ryan, and S. J. Skinner, Energy Environ. Sci. **7**, 311 (2014).

[46] A. Jablonski and C. J. Powell, J. Vac. Sci. Technol. A **27**, 253 (2009).

[47] W. Smekal, W. S. M. Werner, and C. J. Powell, Surf. Interface Anal. **37**, 1059 (2005).

[48] J. B. Goodenough, J. Phys. Chem. Solids **6**, 287 (1958).

[49] J. Kanamori, J. Phys. Chem. Solids **10**, 87 (1959).